

University of Hawai'i 88-inch Telescope Observations of the Interstellar Comet 3I/ATLAS: Spectrophotometric Blue-Sensitive Spectral Time Series Spanning Two Months from Discovery

W. B. HOOGENDAM^{1,*}, D. KUESTERS², B. J. SHAPPEE¹, G. ALDERING³, J. J. WRAY^{4,1}, B. YANG⁵,
K. J. MEECH¹, M. A. TUCKER^{6,7,†}, M. E. HUBER¹, K. AUCHETTL^{8,9}, C. R. ANGUS^{10,11}, D. D. DESAI¹,
J. T. HINKLE^{12,13,‡}, J. KİYOKAWA¹⁴, G. S. H. PAEK¹, S. ROMAGNOLI⁸, J. SHI⁸, A. SYNCATTO^{15,1},
C. ASHALL¹, M. DIXON¹⁵, K. HART¹, A. M. HOFFMAN¹, D. O. JONES¹⁵, K. MEDLER¹, AND C. PFEFFER¹

¹Institute for Astronomy, University of Hawai'i, Honolulu, HI 96822, USA

²Deutsches Elektronen-Synchrotron, Platanenallee 6, 15738 Zeuthen, Germany

³Lawrence Berkeley National Laboratory, 1 Cyclotron Road, MS 50B-4206, Berkeley, CA 94720, USA

⁴School of Earth and Atmospheric Sciences, Georgia Institute of Technology, 311 Ferst Drive, Atlanta, GA 30332, USA

⁵Instituto de Estudios Astrofísicos, Facultad de Ingeniería y Ciencias, Universidad Diego Portales, Santiago, Chile

⁶Center for Cosmology & Astroparticle Physics, The Ohio State University, Columbus, OH, USA

⁷Department of Astronomy, The Ohio State University, Columbus, OH, USA

⁸School of Physics, University of Melbourne, Parkville, VIC 3010, Australia

⁹Department of Astronomy and Astrophysics, University of California, Santa Cruz, CA 93105, USA

¹⁰Astrophysics Research Centre, School of Mathematics and Physics, Queen's University Belfast, Belfast BT7 1NN, UK

¹¹DARK, Niels Bohr Institute, University of Copenhagen, Jagtvej 128, DK-2200 Copenhagen Ø Denmark

¹²Department of Astronomy, University of Illinois Urbana-Champaign, 1002 West Green Street, Urbana, IL 61801, USA

¹³NSF-Simons AI Institute for the Sky (SkAI), 172 E. Chestnut St., Chicago, IL 60611, USA

¹⁴Department of Astronomy, University of Wisconsin, Madison, WI 53706, USA and

¹⁵Institute for Astronomy, University of Hawai'i, 640 N. A'ohoku Pl., Hilo, HI 96720, USA

Version December 11, 2025

ABSTRACT

Interstellar objects are the ejected building blocks of other solar systems. As such, they enable the acquisition of otherwise inaccessible information about nascent extrasolar systems. The discovery of the third interstellar object, 3I/ATLAS, provides an opportunity to explore the properties of a small body from another solar system and to compare it to the small bodies in our own. To that end, we present spectrophotometric observations of 3I/ATLAS taken using the SuperNova Integral Field Spectrograph on the University of Hawai'i 2.2-m telescope. Our data includes the earliest $\lambda \leq 3800$ Å spectrum of 3I/ATLAS, obtained ~ 12.5 hours after the discovery announcement. Later spectra confirm previously reported cometary activity, including Ni and CN emission. The data show wavelength-varying spectral slopes ($S \approx (0\% - 29\%)/1000$ Å, depending on wavelength range) throughout the pre-perihelion ($r_h = 4.4 - 2.5$ au) approach of 3I/ATLAS. We perform synthetic photometry on our spectra and find 3I/ATLAS shows mostly stable color evolution over the period of our observations, with $g - r$ colors ranging from $\sim 0.69 - 0.75$ mag, $r - i$ colors ranging from $\sim 0.26 - 0.30$ mag, and $c - o$ colors ranging from $\sim 0.50 - 0.55$ mag. Ongoing post-perihelion observations of 3I/ATLAS will provide further insight into its potentially extreme composition.

Subject headings: Asteroids(72); Comets(280); Meteors(1041); Interstellar Objects (52); Comet Nuclei (2160); Comet Volatiles (2162); Small Solar System Bodies (1469); Astrochemistry (75); Planetesimals (1259)

1. INTRODUCTION

Comets and asteroids from other solar systems that pass through our own solar system on hyperbolic orbits are nominally common (e.g., Engelhardt et al. 2017; Do et al. 2018), but they are rarely observed. Once discovered, these objects offer a unique and exclusive glimpse into the small bodies of other stellar systems and the physical and chemical processes that lead to their formation (e.g., Jewitt & Seligman 2023). Whereas solar system comets enable the study of primordial material from our own solar system (e.g., Bodewits et al. 2024), interstellar objects perform an analogous function: they enable the study of the primordial material for other solar systems (e.g., Fitzsimmons et al. 2024). Recently, Den-

neau et al. (2025) reported the discovery of a third interstellar object by the Asteroid Terrestrial-impact Last Alert System (ATLAS; Tonry et al. 2018, 2025). This object, named 3I/ATLAS, is merely the third interstellar object, following 1I/'Oumuamua (Meech et al. 2017) and 2I/Borisov (Borisov et al. 2019).

The first two interstellar objects showed disparate properties. Cometary activity, arising from solar radiation heating the surface-layer materials (e.g., Whipple 1950, 1951), differed between the previous two interstellar objects, with 1I/'Oumuamua lacking observed cometary activity (e.g., Meech et al. 2017; Ye et al. 2017; Jewitt et al. 2017; 'Oumuamua ISSI Team et al. 2019; Trilling et al. 2018) and 2I/Borisov showing strong outgassing activity (Fitzsimmons et al. 2019; Jewitt & Luu 2019; Cremonese et al. 2020; Guzik et al. 2020; Hui et al. 2020; Kim et al. 2020; McKay et al. 2020; Ye et al.

*NSF Fellow

†CCAPP Fellow

‡NHFP Einstein Fellow

2020; Yang et al. 2021) and a composition mirroring solar-system comet-like features such as C_2 (Lin et al. 2020), $[O\ I]$ (McKay et al. 2020), OH (Xing et al. 2020), NH_2 (Bannister et al. 2020) species, and Ni outgassing (Guzik et al. 2020; Opitom et al. 2021). While similar to solar system comets in many respects, 2I/Borisov had an unusually high abundance of CO (Bodewits et al. 2020; Cordiner et al. 2020). Both 1I/‘Oumuamua and 2I/Borisov had similar reflectance spectra, with spectral slopes ranging from 5% to 25% per 1000 Å, depending on the wavelength range and data source (for a review, see Jewitt & Seligman 2023).

The recently discovered 3I/ATLAS shows cometary activity like 2I/Borisov (Seligman et al. 2025; Jewitt et al. 2025; Cordiner et al. 2025; Frincke et al. 2025; Rahatgaonkar et al. 2025; Opitom et al. 2025; de la Fuente Marcos et al. 2025; Chandler et al. 2025; Lisse et al. 2025). The initial spectrum from the University of Hawai‘i 2.2-meter (UH 2.2m) telescope and other facilities exhibited a red-sloped reflectance spectrum without strong emission features (Seligman et al. 2025; Opitom et al. 2025; Puzia et al. 2025). As it approached perihelion, outgassing increased. Absorption by water ice grains (Yang et al. 2025) and emission from CN (Rahatgaonkar et al. 2025; Hoogendam et al. 2025a; Salazar Manzano et al. 2025), HCN (Coulson et al. 2025, see also Hinkle et al. 2025a), Ni (Rahatgaonkar et al. 2025; Hoogendam et al. 2025a), Fe (Hutsemékers et al. 2025), CO_2 (Lisse et al. 2025; Cordiner et al. 2025), CO (Cordiner et al. 2025), and OH (Xing et al. 2025) have been reported.

Unlike previous comets, 3I/ATLAS is benefiting from intensive integral field unit (IFU) observations. IFUs offer two advantages over traditional slit spectrographs for comet studies: they enable spatially resolved observations and spectrophotometric flux calibration. Previously reported IFU data on 3I/ATLAS included a spectrum from Opitom et al. (2025), taken shortly (~ 3 hours) after the discovery announcement, by the VLT-mounted Multi Unit Spectroscopic Explorer (MUSE, Bacon et al. 2010). Unfortunately, MUSE lacks the blue wavelength coverage to observe common comet emission features, such as CN. Opitom et al. (2025) used the Wide Field Mode with a $1'$ by $1'$ field of view and a wavelength range of 4800–9200 Å. Additionally, Hoogendam et al. (2025a) presented a Keck Cosmic Web Imager spectrum (Morrissey et al. 2018) obtained nearly two months after discovery. KCWI can observe blue wavelengths, and these data revealed that the Ni emission is more centrally concentrated than the CN emission and the broad-band coma light.

In this manuscript, we present a spectral time series of integral-field unit (IFU) observations of 3I/ATLAS from the SuperNova Integral Field Spectrograph (SNIFS; Lantz et al. 2004) on the UH 2.2m telescope, taken as part of the Spectroscopic Classification of Astronomical Transients (SCAT; Tucker et al. 2022) survey.

2. DATA

Nine spectra were obtained between UT 2025 July 3 and UT 2025 September 2 using the SNIFS instrument on the University of Hawai‘i (UH) 2.2-meter telescope at Maunakea by the SCAT team. A log of the data is presented in Table 1. The SCAT collaboration uses

TABLE 1
Log of spectroscopic observations. r_h is the heliocentric distance, Δ is the geocentric distance, α is the phase angle, and TA is the true anomaly, or position along the orbit.

UT Date	MJD	r_h au	Δ au	α Degrees	TA Degrees
2025-07-03	60859.3	4.43	3.44	2.6	-78.9
2025-07-04	60860.4	4.40	3.40	3.0	-78.7
2025-07-12	60868.4	4.14	3.19	5.9	-77.4
2025-07-14	60870.4	4.07	3.14	6.6	-77.0
2025-07-18	60874.3	3.94	3.06	8.2	-76.3
2025-07-19	60875.3	3.91	3.03	8.6	-66.1
2025-08-18	60905.3	2.94	2.64	20.0	-68.0
2025-08-23	60910.2	2.78	2.61	21.3	-66.2
2025-09-02	60920.6	2.47	2.57	23.0	-61.6

the UH 2.2-meter and the Australian National University 2.3-meter telescopes to classify and spectroscopically follow transient phenomena such as supernovae (e.g., Tucker et al. 2024; Hoogendam et al. 2025b,c), tidal disruption events (e.g., Hinkle et al. 2021, 2023; Hoogendam et al. 2024; Hinkle et al. 2024, 2025b; Pandey et al. 2025), active galactic nuclei (e.g., Neustadt et al. 2023), X-ray binaries (e.g., Tucker et al. 2018), and dipper stars (e.g., Forés-Toribio et al. 2025).

SNIFS contains two channels split by a dichroic mirror. The blue channel covers the 3400–5100 Å range, and the red channel covers 5100–10000 Å. The spectral resolutions are 5 Å and 7 Å, respectively. The data were reduced using the Nearby Supernova Factory (Aldering et al. 2002) reduction pipeline (Bacon et al. 2001; Aldering et al. 2006; Scalzo et al. 2010), and flux calibrated following the steps detailed in Buton et al. (2013). Fluxes were extracted using the Gaussian+Moffat point-spread-function model with a flat background, as described in Rubin et al. (2022). Some of the coma may end up in the sky; however, the flux profile of 3I/ATLAS is dominated by the nucleus (see, e.g., Hoogendam et al. 2025a), so the effect is negligible.

The solar analogue HD 165290 was observed at all epochs except 2025-07-03 and 2025-07-19. For those epochs, we use the observations of HD 165290 from the night before or after, respectively. For the final epoch on 2025-09-02, HD 165290 was unobservable due to a small lunar separation of 4 degrees, so the solar analogue HD 142801 was observed instead. Each final calibrated reflectance spectrum was obtained by dividing the target spectrum by the solar analogue spectrum and normalizing at 5500 Å. Because we use the same solar analogue for all our observations, differences in spectral slope evolution will not be introduced by the solar analogue.

3. ANALYSIS

Figure 1 shows the spectrophotometric time series data presented in this work. The July 3rd spectrum shows a stellar streak that overlaps with the comet, resulting in a different spectral slope in the redder bands. The contaminating stellar source is extinguished by Milky Way dust, reducing the contaminating flux at bluer wavelengths. This makes wavelengths below ~ 6000 Å mostly contamination-free, and our visual inspection of the cubes confirms that 3I/ATLAS is the dominant source of flux at these wavelengths. However, at redder wave-

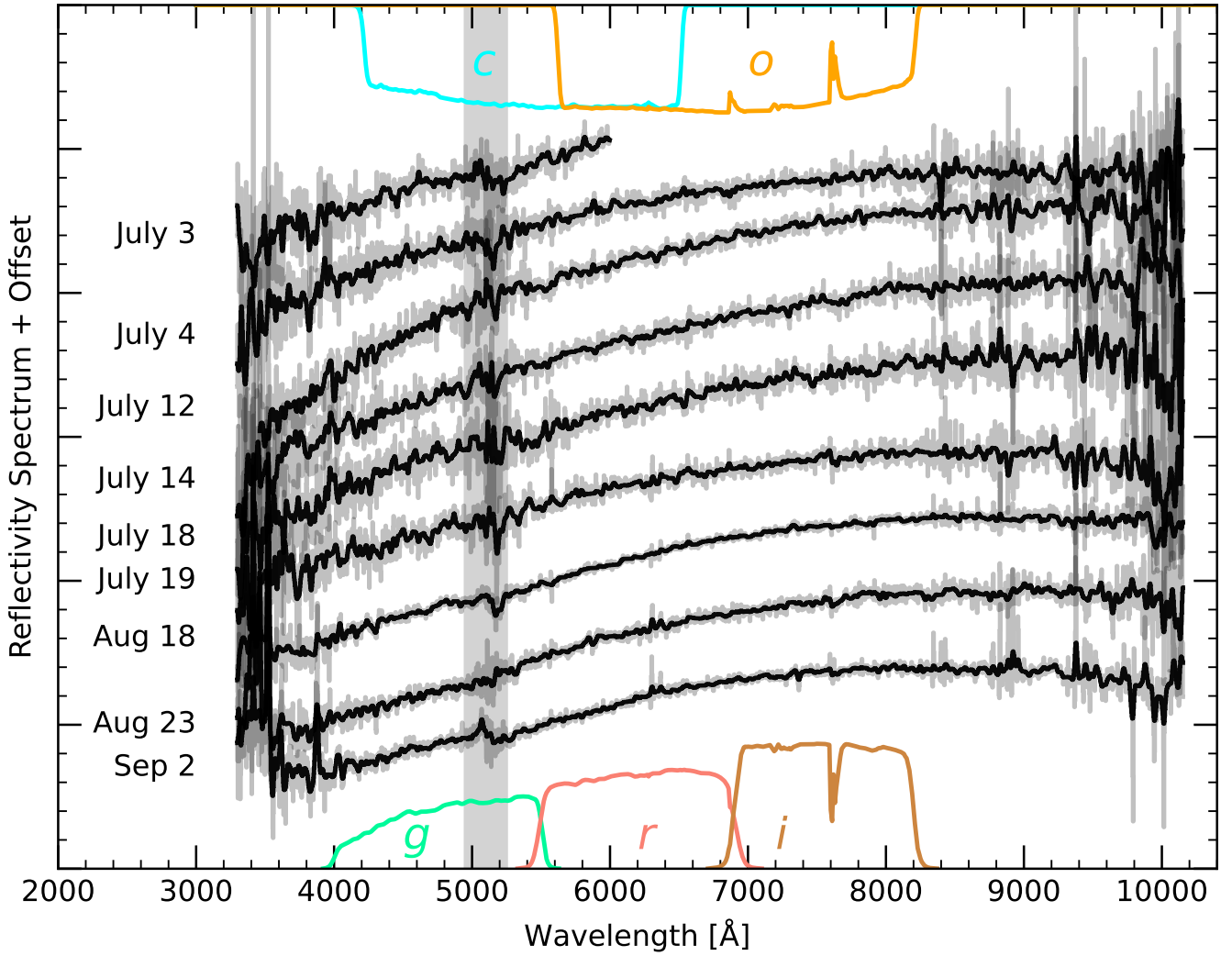


Fig. 1.— The spectrophotometric time series data of 3I/ATLAS from the UH 2.2-meter telescope taken with the SNIFS spectrograph. Grey curves are the original data, and black curves represent the Gaussian-smoothed data. The SNIFS dichroic boundary between ~ 5000 - 5200 Å is shaded grey. The Nearby Supernova Factory pipeline improves the dichroic region; however, some spectra still exhibit low signal-to-noise ratios in that region. The Pan-STARRS (bottom) and ATLAS (top) filter transmission functions are also shown. The red channel of the first spectrum is contaminated by a stellar streak, leading to a slope that differs from those of the other spectra and is therefore excluded. The blue channel is unaffected by the stellar streak because the contaminating star is extinguished by the Milky Way.

lengths the contamination flux is non-negligible, so we mask wavelengths redder than ~ 6000 Å and exclude this spectrum from our spectral slope analysis below.

3.1. Synthetic Photometry

The accurate spectral flux calibration of our SNIFS spectra enables reliable synthetic photometry. The PSF-model fitting prevents exact knowledge of the aperture, but we find in 3.2 that assuming a $3''$ aperture provides a reliable CN production rate and is consistent with IFU data from (Hoogendam et al. 2025a). Table 2 contains a log of our synthetic photometry. The synthetic Pan-STARRS *gri* (Chambers et al. 2016) and ATLAS *co* (Tonry et al. 2018) photometry from photometric nights is plotted in Figure 2, along with previously reported ATLAS photometry from Tonry et al. (2025). Differences in magnitude are expected due to the different apertures used, which will contain different amounts of the cometary coma. Shortly after discovery, the *c*- and

o-band data agree with our synthetic magnitudes, likely due to the cometary activity being entirely encapsulated in both the ATLAS aperture and SNIFS field-of-view. As cometary activity increases, the larger ATLAS apertures capture more cometary flux and thus appear brighter than our values.

3I/ATLAS shows a stable color evolution across most of our observations, with observed $g - r$ colors ranging from 0.69 to 0.75 mag, $r - i$ colors from 0.26 to 0.30 mag, and $c - o$ colors from 0.50 to 0.55 mag. The July 12 and 14 spectra have different colors, but there may be a poorly understood data issue with the July 12 data (see Section 3.3 for further discussion). The measured colors from different groups exhibit systematic variations, likely due to differences in filter bandpasses and aperture sizes, yet each reported color is consistent with a moderately red, dust-dominated coma. Puzia et al. (2025) measured SDSS $g - r = 0.86 \pm 0.05$ mag and Pan-STARRS $g - r = 0.73 \pm 0.05$ mag from July 4 flux-calibrated spectra, and

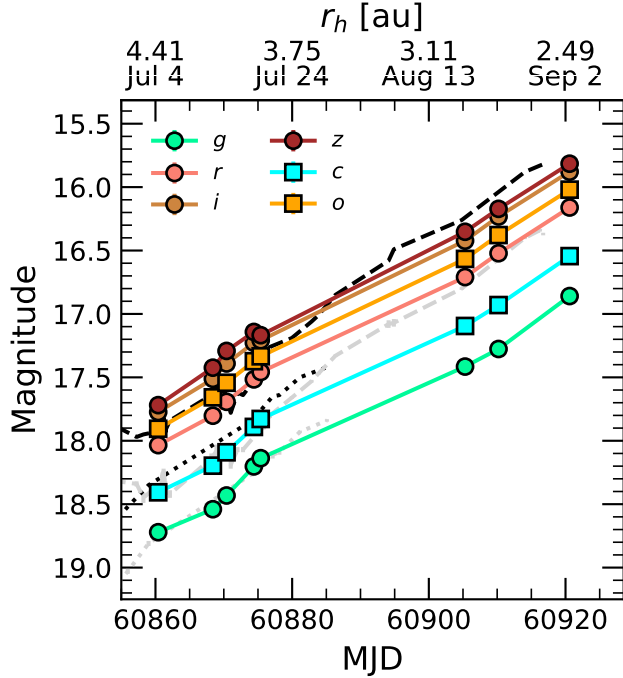


Fig. 2.— Synthetic photometry in the Pan-STARRS *griz* and ATLAS *co* passbands. All magnitudes are reported in the AB system. Reported “m10” ATLAS magnitudes from [Tonry et al. \(2025\)](#) are shown as black lines, and the “m6” ATLAS magnitudes are shown as grey lines. The cyan filter is denoted using dotted lines, and the orange filter is denoted using dashed lines.

[Kareta et al. \(2025\)](#) report $g' - i' = 0.98 \pm 0.03$ mag from IRTF observations using ‘Ophi (Lee et al. 2022), whereas our PSF-extracted IFU data yield slightly bluer values for the Pan-STARRS filters ($g - r \approx 0.69\text{--}0.75$ mag). [Beniyama \(2025\)](#) report slightly bluer colors ($g - r \approx 0.60$ mag, $r - i \approx 0.21$ mag) on July 15, and [Bolin et al. \(2025\)](#) reported $B - V = 0.98 \pm 0.23$ mag, $V - R = 0.71 \pm 0.09$ mag, $g - r = 0.84 \pm 0.05$ mag, $r - i = 0.16 \pm 0.03$ mag.

3.2. Activity

The final three epochs of SNIFS spectra contain emission lines arising from cometary activity (Figure 3). We use the solar analogue to subtract the continuum flux contribution using the same model as [Rahatgaonkar et al. \(2025\)](#) and [Hoogendam et al. \(2025a\)](#). The continuum contribution is modeled as a function of wavelength, defined as

$$F_{\text{cont}}(\lambda) = R(\lambda) \times F_{\odot \text{ analogue}} \left[\lambda \left(1 + \frac{v}{c} \right) + \delta\lambda \right]. \quad (1)$$

The function $R(\lambda)$ is a second-order polynomial $R(\lambda) \equiv \frac{1}{S} (1 + b_1\lambda + b_2\lambda^2)$ that serves as a normalized reflectance function, where the normalization factor S accounts for the flux differences between comet and solar analog. $F_{\odot \text{ analogue}}$ is the shifted solar analogue spectrum. The fitted shift parameters, v and $\delta\lambda$, account for the relative motion between Earth and the comet and between Earth and the solar analogue star. The parameters b_1 and b_2 quantify the reflectance slope. The high signal-to-noise ratio of the solar analogue data results in a negligible contribution to the overall error budget.

We observe CN and Ni I features that have been previ-

TABLE 2
Log of synthetic photometry. Magnitudes are reported in the AB system. See [Tonry et al. \(2018\)](#) for *co* bandpass information and [Chambers et al. \(2016\)](#) for *griz* bandpass information.

UT Date	MJD	r_h	Filter	Magnitude	Magnitude Error
2025-07-04	60860.4	4.40	<i>g</i>	18.72	0.01
2025-07-04	60860.4	4.40	<i>c</i>	18.41	0.01
2025-07-04	60860.4	4.40	<i>r</i>	18.03	0.01
2025-07-04	60860.4	4.40	<i>o</i>	17.91	0.01
2025-07-04	60860.4	4.40	<i>i</i>	17.77	0.01
2025-07-04	60860.4	4.40	<i>z</i>	17.72	0.01
2025-07-12	60868.4	4.14	<i>g</i>	18.54	0.01
2025-07-12	60868.4	4.14	<i>c</i>	18.20	0.01
2025-07-12	60868.4	4.14	<i>r</i>	17.80	0.01
2025-07-12	60868.4	4.14	<i>o</i>	17.66	0.01
2025-07-12	60868.4	4.14	<i>i</i>	17.51	0.01
2025-07-12	60868.4	4.14	<i>z</i>	17.42	0.01
2025-07-14	60870.4	4.07	<i>g</i>	18.43	0.01
2025-07-14	60870.4	4.07	<i>c</i>	18.09	0.01
2025-07-14	60870.4	4.07	<i>r</i>	17.69	0.01
2025-07-14	60870.4	4.07	<i>o</i>	17.54	0.01
2025-07-14	60870.4	4.07	<i>i</i>	17.39	0.01
2025-07-14	60870.4	4.07	<i>z</i>	17.29	0.01
2025-07-18	60874.4	3.94	<i>g</i>	18.20	0.01
2025-07-18	60874.4	3.94	<i>c</i>	17.89	0.01
2025-07-18	60874.4	3.94	<i>r</i>	17.52	0.01
2025-07-18	60874.4	3.94	<i>o</i>	17.37	0.01
2025-07-18	60874.4	3.94	<i>i</i>	17.23	0.01
2025-07-18	60874.4	3.94	<i>z</i>	17.14	0.01
2025-07-19	60875.4	3.91	<i>g</i>	18.14	0.01
2025-07-19	60875.4	3.91	<i>c</i>	17.83	0.01
2025-07-19	60875.4	3.91	<i>r</i>	17.46	0.01
2025-07-19	60875.4	3.91	<i>o</i>	17.33	0.01
2025-07-19	60875.4	3.91	<i>i</i>	17.21	0.01
2025-07-19	60875.4	3.91	<i>z</i>	17.17	0.01
2025-08-18	60905.3	2.94	<i>g</i>	17.41	0.01
2025-08-18	60905.3	2.94	<i>c</i>	17.09	0.01
2025-08-18	60905.3	2.94	<i>r</i>	16.71	0.01
2025-08-18	60905.3	2.94	<i>o</i>	16.57	0.01
2025-08-18	60905.3	2.94	<i>i</i>	16.42	0.01
2025-08-18	60905.3	2.94	<i>z</i>	16.35	0.01
2025-08-23	60910.2	2.78	<i>g</i>	17.28	0.01
2025-08-23	60910.2	2.78	<i>c</i>	16.93	0.01
2025-08-23	60910.2	2.78	<i>r</i>	16.52	0.01
2025-08-23	60910.2	2.78	<i>o</i>	16.38	0.01
2025-08-23	60910.2	2.78	<i>i</i>	16.23	0.01
2025-08-23	60910.2	2.78	<i>z</i>	16.17	0.01
2025-09-02	60920.6	2.47	<i>g</i>	16.86	0.01
2025-09-02	60920.6	2.47	<i>c</i>	16.54	0.01
2025-09-02	60920.6	2.47	<i>r</i>	16.16	0.01
2025-09-02	60920.6	2.47	<i>o</i>	16.02	0.01
2025-09-02	60920.6	2.47	<i>i</i>	15.88	0.01
2025-09-02	60920.6	2.47	<i>z</i>	15.82	0.01

ously reported (e.g., [Rahatgaonkar et al. 2025](#); [Hoogendam et al. 2025a](#)). Additionally, [Hutsemékers et al. \(2025\)](#) report Fe I features emerging after the CN and Ni emission on August 28 and stacked September 3+4. Our September 2nd spectrum may have some emission consistent with the reported Fe I features, but the signal-to-noise ratio of the lines is insufficient to claim a clear detection.

A simple ([Haser 1957](#)) model was used to convert the measured CN line flux into a gas production rate. The number of photons emitted per molecule per second (the so-called g-factor) and the scale lengths were taken from [A’Hearn et al. \(1995\)](#). We assumed that the gas escapes isotropically from the nucleus at a constant velocity, and adopted a mean expansion speed of $0.8 \times r_h^{-0.6}$ km s^{−1}, following [Biver et al. \(1999\)](#), where r_h is the heliocentric distance in au.

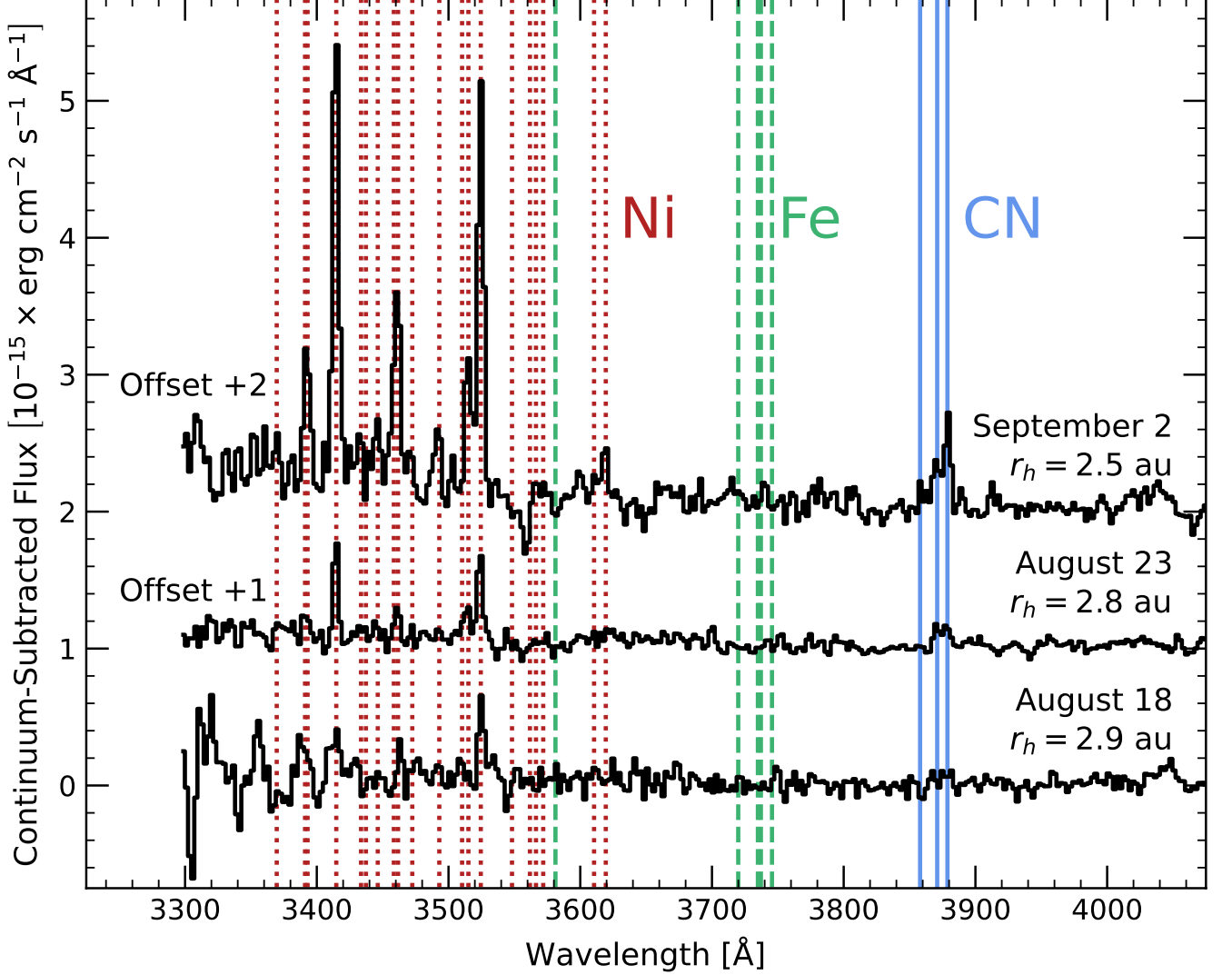


Fig. 3.— The continuum-subtracted spectra showing emission lines from Ni (dotted red), Fe (dashed green), and CN (solid blue).

Because the spectral extraction method for the SNIFS data cubes relies on a PSF model over the entire cube, the exact aperture (or the effective aperture weighted by the PSF that results in an “equivalent noise area” King 1983) over which the spectrum was extracted is non-trivial. Because the angular extent of 3I/ATLAS may vary, such an aperture is not constant and is difficult to use for literature comparisons.

Instead, we report inferred production rates measured from the PSF-extracted spectra assuming two different aperture radii: $2''$ and $3''$. While $2''$ or $3''$ apertures are not constant with respect to the “equivalent noise area”, they at least facilitate a more straightforward literature comparison. The $3''$ values are likely more accurate given the known coma, which extends $\sim 3''$ in the IFU data presented by Hoogendam et al. (2025a). We include $2''$ values for completeness. Our CN production rates are logged in Table 3.

We also report an upper limit of $Q(\text{CN}) < 9.8 \times 10^{23}$ molecules s^{-1} from our highest SNR spectrum, taken on July 12. Our first detection is on August 18

TABLE 3
Log of CN production rates. Table 1 contains orbital properties like heliocentric and geocentric distances.

UT Date	MJD	$3''$ Rate molecules s^{-1}	$2''$ Rate molecules s^{-1}
2025-07-12	60868.4	$< 9.8 \times 10^{23}$...
2025-08-18	60905.3	$(0.8 \pm 0.3) \times 10^{24}$	$(1.8 \pm 0.7) \times 10^{24}$
2025-08-23	60910.2	$(1.2 \pm 0.3) \times 10^{24}$	$(2.5 \pm 0.6) \times 10^{24}$
2025-09-02	60920.6	$(3.1 \pm 0.5) \times 10^{24}$	$(6.5 \pm 1.1) \times 10^{24}$

with a production rate of $(8.4 \pm 3.2) \times 10^{23}$ molecules s^{-1} assuming a $3''$ effective aperture radius.

3.3. Spectral Slopes

For our spectral slope calculations, we divide our spectra by the solar analog spectrum to obtain reflectance spectra, which are normalized to 1 at 5500 Å . We measure the spectral slope for each epoch of 3I/ATLAS using a linear fit to the normalized reflectance spectra over various wavelength ranges, masking wavelengths near the

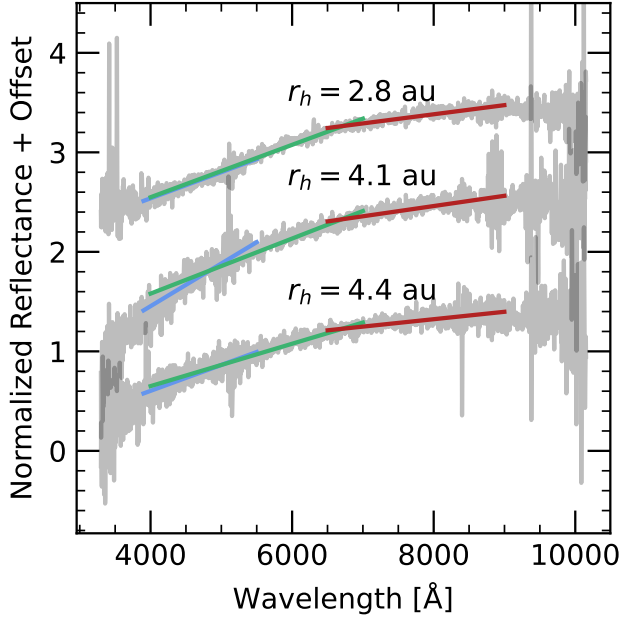


Fig. 4.— The spectral slope evolution fits for several epochs of 3I/ATLAS SNIFS spectra. The different colors represent different fitted wavelength ranges.

SNIFS dichroic crossover. To ensure robust error estimates, we perform 100 bootstrap iterations, randomly sampling 90% of the spectral points in each. Figure 4 shows the spectral slope fits, and Figure 5 shows the spectral slope evolution.

3I/ATLAS exhibits a red reflectance color throughout its spectral evolution, likely due to its dusty coma (Seligman et al. 2025; Opitom et al. 2025; Yang et al. 2025; Kareta et al. 2025; Santana-Ros et al. 2025). From 4000 Å to 7000 Å, the slope of 3I/ATLAS ranges from 20%/1000 Å to 29%/1000 Å. Previously reported spectral slope values for 3I/ATLAS are consistent with our results and are compiled in Table 4.

4. DISCUSSION OF SPECTRAL SLOPE RESULTS

We begin our discussion with remarks on the striking, sudden red slope “spike” from July 12 to 14 ($r_h \approx 4.1$ au). The blue slope on July 12 may likely be an erroneous slope introduced during data reduction. However, we are unable to find the exact cause. The computed instrumental response and atmospheric extinction are similar to those on other nights. While 3I/ATLAS was in a crowded field at the time of observation, we rule out stellar streak contamination for two reasons. First, the July 12th spectrum (shown in Figure 4) is a median of extracted spectral from the 3 uncontaminated exposures of 3I/ATLAS (a fourth exposure was removed due to a visible streak), so any influence from stellar streak contamination should be removed during the coadd. Second, we inspect the white-light images of the cubes and confirm that there is no contaminating streak. An additional check is to compute the spectral slopes using the secondary solar analogue stars. Unfortunately, the spectra of the secondary analog for July 12, HD 157842, and HD 165290 are significantly different. Our spectrum of HD 157842 from July 12 differs from those of HD 165290

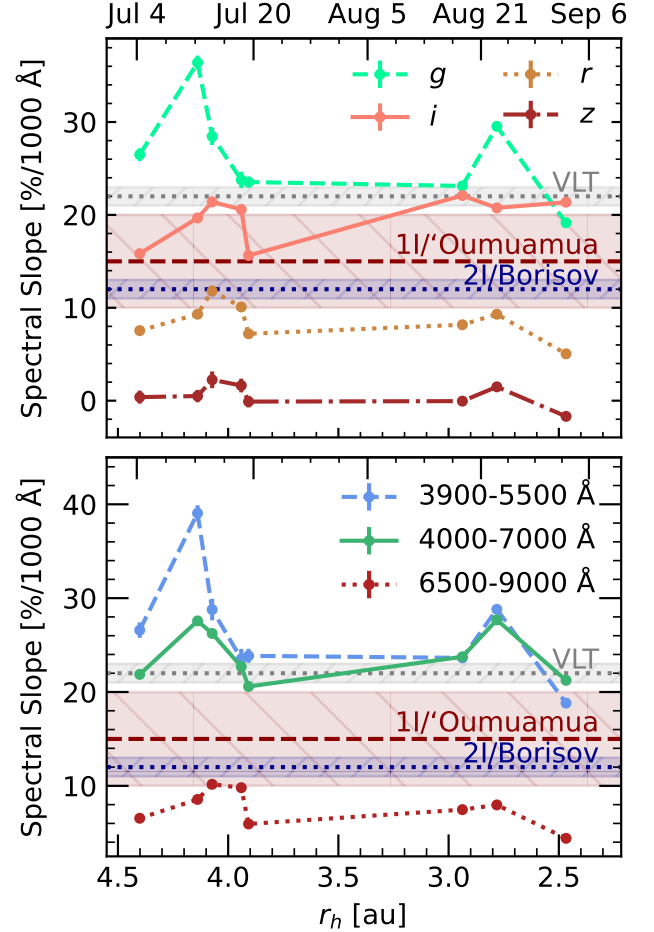


Fig. 5.— The spectral slope evolution for 3I/ATLAS from our SNIFS spectra. The slope is described in the text. We compute the slopes using a linear fit to the reflectance spectra, with values normalized at 5500 Å. The first spectrum is excluded because it lacks uncontaminated red-wavelength coverage. The crosshatched regions centered on the dashed red and dotted blue lines denote the aggregate slope values for 1I/'Oumuamua and 2I/Borisov, respectively, from Jewitt & Seligman (2023). The grey-shaded region shows the spectral slope reported by Rahatgaonkar et al. (2025) for their spectroscopic time-series data from $r_h \approx 4.4$ to 2.9 au. Only statistical uncertainties are plotted. See Section 4 for discussion about the steep red slopes between July 12-14.

from July 12 and 14, and of the secondary solar analogue HD 154805 from July 14. The spectral slopes are consistent using any of these three stars, while the spectral slope using HD 157842 is a mere 17%/1000 Å, far less red than any other measurement we make.

On the other hand, the July 14 spectrum shows a similar slope regardless of which solar analogue star from that night was used. The cube does not show a stellar streak. While the slope remains redder in this epoch, it is likely more reliable than the July 12 measurement, and its variation likely arises from intrinsic systematic scatter in spectral slope measurements.

Unfortunately, there is a dearth of literature measurements during this time phase to compare our spectral slopes. Rahatgaonkar et al. (2025) report spectral slopes from 3900 Å to 5550 Å of 22 ± 1 %/1000 Å for all epochs, which includes an epoch on July 17, but not during the reddest slope epochs we see. As-of-yet un-

TABLE 4
Log of literature spectral slope measurements for 3I/ATLAS.

r_h (au)	Wavelength (Å)	Slope (%/1000Å)
4.40	3900–5500	26.6 ± 0.8^a
4.14	3900–5500	39.1 ± 0.8^a
4.07	3900–5500	28.8 ± 1.1^a
3.94	3900–5500	23.5 ± 1.1^a
3.91	3900–5500	23.9 ± 0.7^a
2.94	3900–5500	23.6 ± 0.3^a
2.78	3900–5500	28.8 ± 0.5^a
2.47	3900–5500	18.8 ± 0.4^a
4.40	4000–5500	27.4 ± 1.0^c
2.80	3900–6000	26.1 ± 0.5^g
3.80	3800–9200	18.3 ± 0.9^f
4.40	4000–7000	17.1 ± 0.2^b
4.40	4000–7000	21.9 ± 0.2^a
4.14	4000–7000	27.6 ± 0.3^a
4.07	4000–7000	26.2 ± 0.3^a
3.94	4000–7000	22.7 ± 0.3^a
3.91	4000–7000	20.6 ± 0.2^a
2.94	4000–7000	23.8 ± 0.1^a
2.78	4000–7000	27.7 ± 0.1^a
2.47	4000–7000	21.2 ± 0.1^a
4.47	5000–7000	18.0 ± 3.0^e
4.40	5500–7000	26.7 ± 0.7^c ; G ² V
4.40	5500–7000	16.4 ± 0.4^c ; SOLSPEC
4.40	5000–8000	11.4 ± 0.2^d
3.80	5000–7000	18.5 ± 0.5^f
2.80	5500–7000	14.0 ± 1.9^g
4.47	7000–9000	17.0 ± 4.0^e
4.40	6500–9000	6.5 ± 0.2^a
4.40	7000–9000	5.2 ± 0.2^d
4.14	6500–9000	8.6 ± 0.2^a
4.07	6500–9000	10.2 ± 0.3^a
4.07	7000–9000	6.7 ± 1.4^d
3.94	6500–9000	9.8 ± 0.3^a
3.91	6500–9000	5.9 ± 0.2^a
3.80	7000–9000	11.6 ± 0.4^f
2.94	6500–9000	7.5 ± 0.1^a
2.80	7000–9000	5.2 ± 0.2^g
2.78	6500–9000	8.0 ± 0.2^a
2.47	6500–9000	4.4 ± 0.1^a

Note. — Spectral slopes are normalized reflectivity gradients typically measured by linear fits to reflectance spectra. Different solar reference spectra and wavelength ranges can lead to systematic differences between measurements. Heliocentric distances (r_h) are approximate values at the time of observation.

^a This work - UH 2.2m/SNIFS

^b Seligman et al. (2025) - SNIFS SCAT pipeline reduction

^c Puzia et al. (2025) - SOAR/Goodman HTS

^d Yang et al. (2025) - Gemini South/GMOS

^e Opitom et al. (2025) - VLT/MUSE

^f de la Fuente Marcos et al. (2025) - GTC/OSIRIS

^g Salazar Manzano et al. (2025) - MDM 2.4m

published VLT/MUSE observations on July 16 are also consistent with our 6500 Å to 9000 Å slope (C. Opitom, private communication). Finally, Jewitt & Luu (2025) obtained photometry from NOT/ALFOSC on July 11, but they do not report spectral slope measurements. As additional observations in this time range are reported, particularly those covering bluer wavelengths, a better understanding of this behavior may emerge.

If this slope trend is real, the rapid change and return may arise from the sublimation of large dust grains, effectively reddening the spectra. Micron-sized icy grains were detected in the spectrum of 3I on July 14 (Yang

et al. 2025). Grains this size near 4 au can live for many days, depending on the albedo (Protopapa et al. 2018). If these ices were embedded in larger refractory grains, once the ices sublimated, only the original red refractory material would be left behind, causing the spectra to return to similar original slopes.

A second, more certain result, is that the redder slopes are flatter than the bluer slopes. This is further evidence to confirm previous speculation that the spectral slopes of 3I/ATLAS may “turn over” at redder wavelengths (e.g., Yang et al. 2025). Indeed, between 8000 Å and 10 000 Å the slopes by eye appear nearly flat, and the 6500 Å to 9000 Å slopes plotted in Figure 5 are far less red and less steep than the bluer wavelength ranges. While similar to the DeMeo et al. (2009) D-type spectral class, those objects do not turn over. The evidence is mounting that 3I/ATLAS turns over in the red wavelengths, as shown by this work and others (e.g., Yang et al. 2025), which is atypical for a comet.

The previous two interstellar objects also had red slopes. The spectral slope for 1I/‘Oumuamua ranged from 7 to 23%/1000 Å (e.g., Jewitt et al. 2017; Meech et al. 2017; Ye et al. 2017; Fitzsimmons et al. 2018), with an average value of (15 ± 5) %/1000 Å (Jewitt & Seligman 2023). Unlike 2I/Borisov and 3I/ATLAS, the spectral slope of 1I/‘Oumuamua reflects the bare nucleus instead of a dusty coma. Of the slope values for 1I/‘Oumuamua, the most similar method is from Meech et al. (2017), who removed the rotation light curve and reported a spectral slope of $\sim 23\%$ /1000 Å, similar to the slope of 3I/ATLAS.

A wide range of spectral slope measurements were reported for 2I/Borisov, with values as low as 5%/1000 Å and as high as 22%/1000 Å, depending on the measurement method and wavelength coverage (e.g., Opitom et al. 2019; Fitzsimmons et al. 2019; Yang et al. 2020; Guzik et al. 2020; Hui et al. 2020; Kareta et al. 2020; de León et al. 2020; Lin et al. 2020; Aravind et al. 2021; Mazzotta Epifani et al. 2021; Prodan et al. 2024; Deam et al. 2025). While a meta-analysis of the spectral slopes of 2I/Borisov is beyond the scope of this work, we highlight the Fitzsimmons et al. (2019) measurement of ~ 20 %/1000 Å for the wavelength range 3900 Å < λ < 6000 Å. The similar wavelength range in our spectrum further supports the claim that 3I/ATLAS is slightly redder than 2I/Borisov.

Overall, 3I/ATLAS appears redder than the previous interstellar objects, likely reflecting compositional and/or particle size differences between it and 1I/‘Oumuamua and 2I/Borisov. All three interstellar objects exhibit colors slightly redder than D-type asteroids (Tholen 1984; DeMeo et al. 2009) but not as red as some outer solar system objects such as 5145/Pholus (Binzel 1992).

It is uncertain if 3I/ATLAS is older than 1I/‘Oumuamua or 2I/Borisov, but its higher velocity may suggest this is the case (e.g., Taylor & Seligman 2025; Hopkins et al. 2025). Hopkins et al. (2025) predicts an older age might correspond to a higher H₂O mass fraction. However, this may contradict the *JWST* data, which showed about the same CO relative to H₂O as 2I/Borisov and much higher CO₂ (never directly measured in 2I/Borisov, see, e.g., McKay et al. 2024)

relative to H₂O compared to almost all solar system comets.

There is an emerging debate in the literature over how much 3I/ATLAS has been changed by space weathering. Yaginuma et al. (2025) present thermal models that suggest 3I/ATLAS preserved a large fraction of its original volatile material; however, Maggiolo et al. (2025) claim significant galactic cosmic ray processing. In any case, space weathering of small bodies in the solar system may redden their surfaces over time (see, e.g., Brunetto et al. 2015) and potentially alter their nuclear composition (e.g., Gronoff et al. 2020; Maggiolo et al. 2020). Some space weathering processes and their relative importance may differ between the solar system and interstellar space, but it seems plausible that the general trend toward reddening over time would be the same. Whether these processes “saturate” on a timescale shorter than billions of years remains an open question, but if not, perhaps 3I/ATLAS’s redder spectrum compared to 1I/Oumuamua and 2I/Borisov could reflect its potentially longer interstellar travel time.

5. COMMENTS ON THE PRE-PERIELION EVOLUTION OF 3I/ATLAS

Our finding of minimal spectral slope evolution between July and September 2025, with spectral slopes ranging from 20–29%/1000 Å and stable $g - r$ colors of 0.69–0.75 mag, may initially appear to contradict reports of dramatic color changes in 3I/ATLAS (e.g., Seligman et al. 2025; Tonry et al. 2025). However, the temporal coverage and activity suggests a two-phase evolutionary model that may reconcile these observations. The first phase, from May ($r_h \approx 5.8$ au) to June ($r_h \approx 3.9$ au) 2025, is a pre-discovery color transition that entails 3I/ATLAS evolving from a plateau into a brightening phase, followed by the second phase of color stability after cometary activity began.

5.1. Preccovery Plateau Through Brightening Phase

During the preccovery plateau phase (May 15–24, 2025, $r_h \approx 5.8$ –5.6 au), the dust-to-nucleus flux ratio remained relatively constant, suggesting steady-state dust production with minimal evolution (Ye et al. 2025). ZTF color measurements during this period were consistent with near-solar colors (Seligman et al. 2025). However, Ye et al. (2025) note that the nucleus contribution represents at most ~17% of the total flux even during this plateau phase, indicating that the object was already actively producing dust. The true nuclear absolute magnitude is constrained at $H_V \gtrsim 15.4$ mag from HST observations (Jewitt et al. 2025), significantly fainter than the $H_V \approx 12.4$ mag measured by ZTF during May, confirming substantial dust contamination even during the apparent color “plateau” phase.

Shortly thereafter (May 27–July 20, 2025, $r_h \approx 5.5$ –3.9 au), a brightening phase began during which the dust-to-nucleus flux ratio linearly increased from at least $F_{\text{dust}}/F_{\text{nucleus}} \approx 5$ to $F_{\text{dust}}/F_{\text{nucleus}} \approx 15$ over ~50 days (Ye et al. 2025). This uniform brightening phase is characterized by a steep heliocentric distance dependence of $\propto r_h^{-3.8}$, significantly steeper than 2I/Borisov ($\propto r_h^{-2.1}$) and more consistent with dynamically old Solar System comets (Ye et al. 2025). Rubin Observatory/LSST preccovery observations (from June 21, 2025, at $r_h = 4.85$ au)

provide further early-time evidence of detected cometary activity with a clearly resolved dust coma (Chandler et al. 2025).

The dramatic color reddening observed by Seligman et al. (2025) occurred during this uniform brightening phase. However, Puzia et al. (2025) caution that the opposition effect at such low phase angles could partially or entirely explain the apparent color evolution between May and June (see, e.g., Rosenbush et al. 2009), complicating the interpretation of the early color measurements. By the time of discovery, observations showed clear evidence of reddening and a resolved coma; the opposition effect alone cannot account for the observed red colors (Puzia et al. 2025; Opitom et al. 2025; Seligman et al. 2025). Based on combined ZTF (Ye et al. 2025) and TESS (Feinstein et al. 2025; Martinez-Palomera et al. 2025) preccovery observations, Ye et al. (2025) infer that constant dust outflow began ~30 days before the preccovery detections in early April at a distance of $r_h \approx 7.5$ au¹.

5.2. Stable Color Phase

Our spectral time series, spanning from July 3, 2025 ($r_h \approx 4.2$ au) to September 2, 2025 ($r \approx 2.0$ au), samples the object after most of the major color transition has completed. Throughout this 2-month period, we observe consistently red spectral slopes (20–29%/1000 Å) and stable colors ($g - r = 0.69$ –0.75 mag, $r - i = 0.26$ –0.30 mag, $c - o = 0.50$ –0.55 mag), excluding the July 12–14 data.

This color stability persists despite clear evidence of evolving cometary activity during the spectral time series. Water activity was first marginally detected via OH emission at 3085 Å by Xing et al. (2025) using *Swift*/UVOT on July 31 at $r_h \approx 3.5$ au. Their derived water production rate implies an active area of at least 7.8 km². Such an area, if confined to the nucleus surface, would require more than 8% of it to be active, a larger fraction than observed for most Solar System comets (Xing et al. 2025). Near-infrared spectroscopy revealed the presence of icy grains in the coma, potentially serving as an extended source of water vapor (Yang et al. 2025; Xing et al. 2025).

CN emission was absent in early July spectroscopy (Seligman et al. 2025; Puzia et al. 2025; de la Fuente Marcos et al. 2025), with the first detections of CN in mid-August (Salazar Manzano et al. 2025; Rahatgaonkar et al. 2025; Hoogendam et al. 2025a), preceded by emerging Ni emission features (Rahatgaonkar et al. 2025; Hoogendam et al. 2025a) and followed by emerging Fe emission features (Hutsemékers et al. 2025). JWST NIRSpec observations revealed a CO₂-dominated coma at $r_h = 3.3$ au, along with detections of H₂O, CO, OCS, water ice absorption, and dust continuum (Cordiner et al. 2025; Yang et al. 2025). The measured CO₂/H₂O ratio is larger than average. This contrasts Solar System comets and provides strong evidence for CO₂-driven activity. Dust production rates also increased over this time frame (Salazar Manzano et al. 2025). Despite these activity changes, the spectral slope remained stable throughout August and into September in our observations.

¹ We correct the original Ye et al. (2025) manuscript distance, which was erroneously stated as 9 au.

5.3. A Potential Physical Explanation

The two-stage evolution (plateau followed by uniform brightening) suggests distinct physical regimes: The plateau phase (May 15–24, 2025, $r_h \approx 5.8$ –5.6 au) likely represents an initial phase in which dust production had reached quasi-equilibrium between sublimation-driven ejection and geometric dilution. The near-solar colors measured during this phase require careful interpretation, given: (1) dust already dominated the brightness (Ye et al. 2025), (2) the measurements were obtained at low phase angles where opposition effects can significantly brighten and alter colors (Rosenbush et al. 2009; Puzia et al. 2025), and (3) uncertainties may be underestimated during the plateau phase due to crowded-field photometry complications (e.g., Ye et al. 2025).

One potential explanation is that 3I/ATLAS exhibited continuous dust production, potentially dating back as far as $r_h \approx 7.5$ au, (early April 2025) (Ye et al. 2025), rather than a sudden transition from an inactive nucleus to a dusty coma. Activity could have potentially started even earlier than $r_h \approx 7.5$ au: JWST detected CO and CO₂ at $r_h = 3.32$ au (Cordiner et al. 2025), and both species sublimate further out than ~ 8 au. The surface sublimation of CO₂ typically begins at ~ 17 –20 au and CO sublimation beyond the Kuiper belt for solar system comets.

The uniform brightening marks a transition where the dust production in 3I/ATLAS increases. The steep brightening law ($\propto r_h^{-3.8}$) is characteristic of dynamically old Solar System comets, consistent with the inferred old age of 3–11 Gyr (Hopkins et al. 2025; Taylor & Seligman 2025; Jewitt & Luu 2025). The reddening occurred as dust production increased, with the red color likely arising from an increasingly dominant refractory organic component in the larger dust population (see, e.g., Levasseur-Regourd et al. 2018). These observations suggest that 3I/ATLAS was continuously active from as early as April ($r_h \approx 7.5$ au) through discovery. This activity is likely an evolution from low-level to high-level dust production, with associated changes in either dust properties (like grain size) or observational effects (including phase angle) producing the observed color evolution.

After its discovery in early July, 3I/ATLAS maintained a consistently red color despite continued evolution in gas emission and dust production. This apparent paradox can be explained if the spectral slope is primarily determined by the optical properties and size distribution of the entrained dust, which remains relatively constant once a steady-state balance is achieved between dust production and removal. The slope change observed between July 12–14 in our spectral time series may coincide with a brief change in dust properties with large dust grains lifted through micron-sized H₂O ice grain sublimation. Outside of the July 12–14 window, the spectral slope during this stage (20–29%/1000 Å in our measurements) is consistent with typical cometary dust continua (Protopapa et al. 2018; Kareta et al. 2023; Kolokolova et al. 2024) and slightly redder than D-type asteroids (DeMeo et al. 2009), suggesting a dust population dominated by sub-micron to micron-sized particles with significant refractory organic content.

The increasing emission from CN, Ni, and Fe, along

with the rising dust production rates observed between August and September, do not produce measurable color changes because these quantities scale together, maintaining a relatively constant dust-to-gas ratio and particle size distribution. Salazar Manzano et al. (2025) measured $\log(Q(\text{CN})/Af\rho) \approx 22.4$, consistent with typical gas-to-dust ratios in active comets, suggesting that the dust and gas production are coupled through a common sublimation-driven mechanism.

6. CONCLUSIONS

We present spectrophotometric data taken using the SNIFS spectrograph on the UH 2.2-meter telescope. Our spectral time series comprises nine spectra spanning the first two months of 3I/ATLAS after discovery, with a wavelength range of 3200 Å to 10000 Å. Our observations span from shortly after the discovery announcement (~ 12.5 hours) to early September, and cover the beginning of optical gas emission activity, contributing to worldwide efforts to characterize 3I/ATLAS.

Our deepest upper limit is on July 12, with $Q(\text{CN}) < 9.8 \times 10^{23}$ molecules s⁻¹. We report a weak detection of CN on August 18 with a production rate of $(8.4 \pm 3.2) \times 10^{23}$ molecules s⁻¹ using a 3'' aperture radius. We subsequently detected CN on August 23 and September 2. Our CN production rate estimates are consistent with other studies (e.g., Rahatgaonkar et al. 2025; Hoogendam et al. 2025a; Salazar Manzano et al. 2025). We also observe previously reported Ni emission (Rahatgaonkar et al. 2025; Hoogendam et al. 2025a). We may barely detect the Fe emission reported in Hutsemékers et al. (2025) in our September 2 spectrum, but the detection would be marginal at best.

The spectral slope of 3I/ATLAS is neutral to red with values from 0%/1000 Å to 29%/1000 Å, depending on the measured wavelength. At the bluer wavelengths, e.g., the *g* band, there is a steep red slope, whereas at redder wavelengths, e.g., in the *z* band, the slope is nearly flat. This slope is generally redder than reported slopes for 1I/Oumuamua and 2I/Borisov.

Comparing the spectral properties of the interstellar comets 1I/Oumuamua, 2I/Borisov, and 3I/ATLAS to those of analogous small bodies in our own solar system (active and dormant comets, asteroids, Trans-Neptunian Objects, etc.) provides heuristic power to evaluate solar system and planetary formation models. Continued post-perihelion photometric and spectroscopic follow-up will further illuminate this exciting interstellar interloper and provide additional insights into its history, evolution, and composition.

We thank John Noonan, Theodore Kareta, Daniela Iglesias, Cyrielle Opitom, and Javier Licandro for helpful discussions about 3I/ATLAS and this manuscript.

W.B.H. acknowledges support from the NSF Graduate Research Fellowship Program under Grant No. 2236415.

The Shapsee group at the University of Hawai'i is supported with funds from NSF (grant AST-2407205) and NASA (grants HST-GO-17087, 80NSSC24K0521, 80NSSC24K0490, 80NSSC23K1431).

This work was supported in part by the Director, Office of Science, Office of High Energy Physics of the U.S.

Department of Energy under Contract No. DE-AC02-05CH11231

K.J.M., J.J.W., and A.H. acknowledge support from the Simons Foundation through SFI-PD-Pivot Mentor-00009672.

J.T.H. acknowledges support from NASA through the NASA Hubble Fellowship grant HST-HF2-51577.001-A, awarded by STScI. STScI is operated by the Association of Universities for Research in Astronomy, Incorporated, under NASA contract NAS5-26555.

REFERENCES

- A'Hearn, M. F., Millis, R. C., Schleicher, D. O., Osip, D. J., & Birch, P. V. 1995, *Icarus*, 118, 223, doi: [10.1006/icar.1995.1190](#)
- Aldering, G., Adam, G., Antilogus, P., et al. 2002, in Society of Photo-Optical Instrumentation Engineers (SPIE) Conference Series, Vol. 4836, Survey and Other Telescope Technologies and Discoveries, ed. J. A. Tyson & S. Wolff, 61–72, doi: [10.1117/12.458107](#)
- Aldering, G., Antilogus, P., Bailey, S., et al. 2006, *ApJ*, 650, 510, doi: [10.1086/507020](#)
- Aravind, K., Ganesh, S., Venkataramani, K., et al. 2021, *MNRAS*, 502, 3491, doi: [10.1093/mnras/stab084](#)
- Bacon, R., Copin, Y., Monnet, G., et al. 2001, *MNRAS*, 326, 23, doi: [10.1046/j.1365-8711.2001.04612.x](#)
- Bacon, R., Accardo, M., Adjali, L., et al. 2010, in Society of Photo-Optical Instrumentation Engineers (SPIE) Conference Series, Vol. 7735, Ground-based and Airborne Instrumentation for Astronomy III, ed. I. S. McLean, S. K. Ramsay, & H. Takami, 773508, doi: [10.1117/12.856027](#)
- Bannister, M. T., Opitom, C., Fitzsimmons, A., et al. 2020, arXiv e-prints, arXiv:2001.11605, <https://arxiv.org/abs/2001.11605>
- Beniyama, J. 2025, *PASJ*, doi: [10.1093/pasj/psaf097](#)
- Binzel, R. P. 1992, *Icarus*, 99, 238, doi: [10.1016/0019-1035\(92\)90185-A](#)
- Biver, N., Bockelée-Morvan, D., Crovisier, J., et al. 1999, *AJ*, 118, 1850, doi: [10.1086/301033](#)
- Bodewits, D., Bonev, B. P., Cordiner, M. A., & Villanueva, G. L. 2024, in Comets III, ed. K. J. Meech, M. R. Combi, D. Bockelée-Morvan, S. N. Raymodn, & M. E. Zolensky (University of Arizona Press), 407–432, doi: [10.2458/azu_uapress_9780816553631-ch013](#)
- Bodewits, D., Noonan, J. W., Feldman, P. D., et al. 2020, *Nature Astronomy*, 4, 867, doi: [10.1038/s41550-020-1095-2](#)
- Bolin, B. T., Belyakov, M., Fremling, C., et al. 2025, *MNRAS*, 542, L139, doi: [10.1093/mnras/131af078](#)
- Borisov, G., Durig, D. T., Sato, H., et al. 2019, *Central Bureau Electronic Telegrams*, 4666, 1
- Brunetto, R., Loeffler, M. J., Nesvorný, D., Sasaki, S., & Strazzulla, G. 2015, in Asteroids IV, ed. P. Michel, F. E. DeMeo, & W. F. Bottke, 597–616, doi: [10.2458/azu_uapress_9780816532131-ch031](#)
- Buton, C., Copin, Y., Aldering, G., et al. 2013, *A&A*, 549, A8, doi: [10.1051/0004-6361/201219834](#)
- Chambers, K. C., Magnier, E. A., Metcalfe, N., et al. 2016, arXiv e-prints, arXiv:1612.05560, doi: [10.48550/arXiv.1612.05560](#)
- Chandler, C. O., Bernardinelli, P. H., Jurić, M., et al. 2025, arXiv e-prints, arXiv:2507.13409, doi: [10.48550/arXiv.2507.13409](#)
- Cordiner, M. A., Milam, S. N., Biver, N., et al. 2020, *Nature Astronomy*, 4, 861, doi: [10.1038/s41550-020-1087-2](#)
- Cordiner, M. A., Roth, N. X., Kelley, M. S. P., et al. 2025, arXiv e-prints, arXiv:2508.18209, doi: [10.48550/arXiv.2508.18209](#)
- Coulson, I. M., Kuan, Y.-J., Charnley, S. B., et al. 2025, arXiv e-prints, arXiv:2510.02817, doi: [10.48550/arXiv.2510.02817](#)
- Cremonese, G., Fulle, M., Cambianica, P., et al. 2020, *ApJ*, 893, L12, doi: [10.3847/2041-8213/ab8455](#)
- de la Fuente Marcos, R., Alarcon, M. R., Licandro, J., et al. 2025, *A&A*, 700, L9, doi: [10.1051/0004-6361/202556439](#)
- de León, J., Licandro, J., de la Fuente Marcos, C., et al. 2020, *MNRAS*, 495, 2053, doi: [10.1093/mnras/staa1190](#)
- Deam, S. E., Bannister, M. T., Opitom, C., et al. 2025, arXiv e-prints, arXiv:2507.05051, doi: [10.48550/arXiv.2507.05051](#)
- DeMeo, F. E., Binzel, R. P., Slivan, S. M., & Bus, S. J. 2009, *Icarus*, 202, 160, doi: [10.1016/j.icarus.2009.02.005](#)
- Denneau, L., Siverd, R., Tonry, J., et al. 2025, *MPEC*
- Do, A., Tucker, M. A., & Tonry, J. 2018, *ApJ*, 855, L10, doi: [10.3847/2041-8213/aaae67](#)
- Engelhardt, T., Jedicke, R., Vereš, P., et al. 2017, *AJ*, 153, 133, doi: [10.3847/1538-3881/aa5c8a](#)
- Feinstein, A. D., Noonan, J. W., & Seligman, D. Z. 2025, *ApJ*, 991, L2, doi: [10.3847/2041-8213/adfd4d](#)
- Fitzsimmons, A., Meech, K., Matrà, L., & Pfalzner, S. 2024, in Comets III, ed. K. J. Meech, M. R. Combi, D. Bockelée-Morvan, S. N. Raymodn, & M. E. Zolensky, 731–766
- Fitzsimmons, A., Snodgrass, C., Rozitis, B., et al. 2018, *Nature Astronomy*, 2, 133, doi: [10.1038/s41550-017-0361-4](#)
- Fitzsimmons, A., Hainaut, O., Meech, K. J., et al. 2019, *ApJ*, 885, L9, doi: [10.3847/2041-8213/ab49fc](#)
- Forés-Toribio, R., JoHantgen, B., Kochanek, C. S., et al. 2025, *The Open Journal of Astrophysics*, 8, 114, doi: [10.33232/001c.143105](#)
- Frincke, T. T., Yaginuma, A., Noonan, J. W., et al. 2025, arXiv e-prints, arXiv:2509.02813, doi: [10.48550/arXiv.2509.02813](#)
- Gronoff, G., Maggiolo, R., Cessateur, G., et al. 2020, *ApJ*, 890, 89, doi: [10.3847/1538-4357/ab67b9](#)
- Guzik, P., Drahus, M., Rusek, K., et al. 2020, *Nature Astronomy*, 4, 53, doi: [10.1038/s41550-019-0931-8](#)
- Haser, L. 1957, *Bulletin de la Societe Royale des Sciences de Liege*, 43, 740
- Hinkle, J. T., Yang, B., Meech, K. J., et al. 2025a, arXiv e-prints, arXiv:2512.02106, <https://arxiv.org/abs/2512.02106>
- Hinkle, J. T., Holoien, T. W. S., Auchettl, K., et al. 2021, *MNRAS*, 500, 1673, doi: [10.1093/mnras/staa3170](#)
- Hinkle, J. T., Tucker, M. A., Shappee, B. J., et al. 2023, *MNRAS*, 519, 2035, doi: [10.1093/mnras/stac3659](#)
- Hinkle, J. T., Auchettl, K., Hoogendam, W. B., et al. 2024, arXiv e-prints, arXiv:2412.15326, doi: [10.48550/arXiv.2412.15326](#)
- Hinkle, J. T., Shappee, B. J., Auchettl, K., et al. 2025b, *Science Advances*, 11, eadt0074, doi: [10.1126/sciadv.adt0074](#)
- Hoogendam, W. B., Hinkle, J. T., Shappee, B. J., et al. 2024, *MNRAS*, 530, 4501, doi: [10.1093/mnras/stae1121](#)
- Hoogendam, W. B., Shappee, B. J., Wray, J. J., et al. 2025a, arXiv e-prints, arXiv:2510.11779, <https://arxiv.org/abs/2510.11779>
- Hoogendam, W. B., Jones, D. O., Ashall, C., et al. 2025b, *The Open Journal of Astrophysics*, 8, 120, doi: [10.33232/001c.143462](#)
- Hoogendam, W. B., Ashall, C., Jones, D. O., et al. 2025c, *ApJ*, 988, 209, doi: [10.3847/1538-4357/ade787](#)
- Hopkins, M. J., Dorsey, R. C., Forbes, J. C., et al. 2025, *From a Different Star: 3I/ATLAS in the context of the Ōtautahi-Oxford interstellar object population model*, <https://arxiv.org/abs/2507.05318>
- Hui, M.-T., Ye, Q.-Z., Föhning, D., Hung, D., & Tholen, D. J. 2020, *AJ*, 160, 92, doi: [10.3847/1538-3881/ab9df8](#)
- Hutsemekers, D., Manfroid, J., Jehin, E., et al. 2025, arXiv e-prints, arXiv:2509.26053, doi: [10.48550/arXiv.2509.26053](#)
- Jewitt, D., Hui, M.-T., Mutchler, M., Kim, Y., & Agarwal, J. 2025, *ApJ*, 990, L2, doi: [10.3847/2041-8213/adf8d8](#)
- Jewitt, D., & Luu, J. 2019, *ApJ*, 886, L29, doi: [10.3847/2041-8213/ab530b](#)
- , 2025, *ApJ*, 994, L3, doi: [10.3847/2041-8213/ae1832](#)
- Jewitt, D., Luu, J., Rajagopal, J., et al. 2017, *ApJL*, 850, L36, doi: [10.3847/2041-8213/aa9b2f](#)
- Jewitt, D., & Seligman, D. Z. 2023, *ARA&A*, 61, 197, doi: [10.1146/annurev-astro-071221-054221](#)
- Kareta, T., Noonan, J. W., Harris, W. M., & Springmann, A. 2023, *PSJ*, 4, 85, doi: [10.3847/PSJ/acc28](#)
- Kareta, T., Andrews, J., Noonan, J. W., et al. 2020, *ApJ*, 889, L38, doi: [10.3847/2041-8213/ab6a08](#)
- Kareta, T., Champagne, C., McClure, L., et al. 2025, arXiv e-prints, arXiv:2507.12234, <https://arxiv.org/abs/2507.12234>
- Kim, Y., Jewitt, D., Mutchler, M., et al. 2020, *ApJ*, 895, L34, doi: [10.3847/2041-8213/ab9228](#)
- King, I. R. 1983, *PASP*, 95, 163, doi: [10.1086/131139](#)
- Kolokolova, L., Kelley, M. S. P., Kimura, H., & Hoang, T. 2024, in Comets III, ed. K. J. Meech, M. R. Combi, D. Bockelée-Morvan, S. N. Raymodn, & M. E. Zolensky, 621–652, doi: [10.2458/azu_uapress_9780816553631-ch019](#)
- Lantz, B., Aldering, G., Antilogus, P., et al. 2004, in Society of Photo-Optical Instrumentation Engineers (SPIE) Conference Series, Vol. 5249, Optical Design and Engineering, ed. L. Mazuray, P. J. Rogers, & R. Wartmann, 146–155, doi: [10.1117/12.512493](#)
- Lee, E., Emerson, K. S., Connelley, M. S., et al. 2022, in Society of Photo-Optical Instrumentation Engineers (SPIE) Conference Series, Vol. 12184, Ground-based and Airborne Instrumentation for Astronomy IX, ed. C. J. Evans, J. J. Bryant, & K. Motohara, 121848D, doi: [10.1117/12.262727](#)
- Levasseur-Regourd, A.-C., Agarwal, J., Cottin, H., et al. 2018, *Space Sci. Rev.*, 214, 64, doi: [10.1007/s11214-018-0496-3](#)

- Lin, H. W., Lee, C.-H., Gerdes, D. W., et al. 2020, *ApJ*, 889, L30, doi: [10.3847/2041-8213/ab6bd9](https://doi.org/10.3847/2041-8213/ab6bd9)
- Lisse, C. M., Bach, Y. P., Bryan, S., et al. 2025, arXiv e-prints, arXiv:2508.15469, doi: [10.48550/arXiv.2508.15469](https://doi.org/10.48550/arXiv.2508.15469)
- Maggiolo, R., Dhooghe, F., Gronoff, G., de Keyser, J., & Cessateur, G. 2025, arXiv e-prints, arXiv:2510.26308, doi: [10.48550/arXiv.2510.26308](https://doi.org/10.48550/arXiv.2510.26308)
- Maggiolo, R., Gronoff, G., Cessateur, G., et al. 2020, *ApJ*, 901, 136, doi: [10.3847/1538-4357/abacc3](https://doi.org/10.3847/1538-4357/abacc3)
- Martinez-Palomera, J., Tuson, A., Hedges, C., et al. 2025, arXiv e-prints, arXiv:2508.02499, doi: [10.48550/arXiv.2508.02499](https://doi.org/10.48550/arXiv.2508.02499)
- Mazzotta Epifani, E., Dotto, E., Perna, D., et al. 2021, *Planet. Space Sci.*, 208, 105341, doi: [10.1016/j.pss.2021.105341](https://doi.org/10.1016/j.pss.2021.105341)
- McKay, A., Opitom, C., Jehin, E., et al. 2024, in *AAS/Division for Planetary Sciences Meeting Abstracts*, Vol. 56, 56th Annual Meeting of the Division for Planetary Sciences, 301.01
- McKay, A. J., Cochran, A. L., Dello Russo, N., & DiSanti, M. A. 2020, *ApJ*, 889, L10, doi: [10.3847/2041-8213/ab64ed](https://doi.org/10.3847/2041-8213/ab64ed)
- Meech, K. J., Weryk, R., Micheli, M., et al. 2017, *Nature*, 552, 378, doi: [10.1038/nature25020](https://doi.org/10.1038/nature25020)
- Morrissey, P., Matuszewski, M., Martin, D. C., et al. 2018, *ApJ*, 864, 93, doi: [10.3847/1538-4357/aad597](https://doi.org/10.3847/1538-4357/aad597)
- Neustadt, J. M. M., Hinkle, J. T., Kochanek, C. S., et al. 2023, *MNRAS*, 521, 3810, doi: [10.1093/mnras/stad725](https://doi.org/10.1093/mnras/stad725)
- Opitom, C., Fitzsimmons, A., Jehin, E., et al. 2019, *A&A*, 631, L8, doi: [10.1051/0004-6361/201936959](https://doi.org/10.1051/0004-6361/201936959)
- Opitom, C., Jehin, E., Hutsemékers, D., et al. 2021, *A&A*, 650, L19, doi: [10.1051/0004-6361/202141245](https://doi.org/10.1051/0004-6361/202141245)
- Opitom, C., Snodgrass, C., Jehin, E., et al. 2025, arXiv e-prints, arXiv:2507.05226, doi: [10.48550/arXiv.2507.05226](https://doi.org/10.48550/arXiv.2507.05226)
- Oumuamua ISSI Team, Bannister, M. T., Bhandare, A., et al. 2019, *Nature Astronomy*, 3, 594, doi: [10.1038/s41550-019-0816-x](https://doi.org/10.1038/s41550-019-0816-x)
- Pandey, P., Hinkle, J., Kochanek, C., et al. 2025, arXiv e-prints, arXiv:2509.03593, doi: [10.48550/arXiv.2509.03593](https://doi.org/10.48550/arXiv.2509.03593)
- Prodan, G. P., Popescu, M., Licandro, J., et al. 2024, *MNRAS*, 529, 3521, doi: [10.1093/mnras/stae539](https://doi.org/10.1093/mnras/stae539)
- Protopapa, S., Kelley, M. S. P., Yang, B., et al. 2018, *ApJ*, 862, L16, doi: [10.3847/2041-8213/aad33b](https://doi.org/10.3847/2041-8213/aad33b)
- Puzia, T. H., Rahatgaonkar, R., Carvajal, J. P., Nayak, P. K., & Luco, B. 2025, arXiv e-prints, arXiv:2508.02777, doi: [10.48550/arXiv.2508.02777](https://doi.org/10.48550/arXiv.2508.02777)
- Rahatgaonkar, R., Carvajal, J. P., Puzia, T. H., et al. 2025, arXiv e-prints, arXiv:2508.18382, doi: [10.48550/arXiv.2508.18382](https://doi.org/10.48550/arXiv.2508.18382)
- Rosenbush, V. K., Shevchenko, V. G., Kiselev, N. N., et al. 2009, *Icarus*, 201, 655, doi: [10.1016/j.icarus.2009.01.007](https://doi.org/10.1016/j.icarus.2009.01.007)
- Rubin, D., Aldering, G., Antilogus, P., et al. 2022, *ApJS*, 263, 1, doi: [10.3847/1538-4365/ac7b7f](https://doi.org/10.3847/1538-4365/ac7b7f)
- Salazar Manzano, L. E., Lin, H. W., Taylor, A. G., et al. 2025, arXiv e-prints, arXiv:2509.01647, doi: [10.48550/arXiv.2509.01647](https://doi.org/10.48550/arXiv.2509.01647)
- Santana-Ros, T., Ivanova, O., Mykhailova, S., et al. 2025, *A&A*, 702, L3, doi: [10.1051/0004-6361/202556717](https://doi.org/10.1051/0004-6361/202556717)
- Scalzo, R. A., Aldering, G., Antilogus, P., et al. 2010, *ApJ*, 713, 1073, doi: [10.1088/0004-637X/713/2/1073](https://doi.org/10.1088/0004-637X/713/2/1073)
- Seligman, D. Z., Micheli, M., Farnocchia, D., et al. 2025, *ApJ*, 989, L36, doi: [10.3847/2041-8213/adf49a](https://doi.org/10.3847/2041-8213/adf49a)
- Taylor, A. G., & Seligman, D. Z. 2025, arXiv e-prints, arXiv:2507.08111, <https://arxiv.org/abs/2507.08111>
- Tholen, D. J. 1984, PhD thesis, University of Arizona
- Tonry, J., Denneau, L., Alarcon, M., et al. 2025, arXiv e-prints, arXiv:2509.05562, doi: [10.48550/arXiv.2509.05562](https://doi.org/10.48550/arXiv.2509.05562)
- Tonry, J. L., Denneau, L., Heinze, A. N., et al. 2018, *PASP*, 130, 064505, doi: [10.1088/1538-3873/aabadf](https://doi.org/10.1088/1538-3873/aabadf)
- Trilling, D. E., Mommert, M., Hora, J. L., et al. 2018, *AJ*, 156, 261
- Tucker, M. A., Shappee, B. J., Holoién, T. W. S., et al. 2018, *ApJ*, 867, L9, doi: [10.3847/2041-8213/aae88a](https://doi.org/10.3847/2041-8213/aae88a)
- Tucker, M. A., Shappee, B. J., Huber, M. E., et al. 2022, *PASP*, 134, 124502, doi: [10.1088/1538-3873/aca719](https://doi.org/10.1088/1538-3873/aca719)
- Tucker, M. A., Hinkle, J., Angus, C. R., et al. 2024, *ApJ*, 976, 178, doi: [10.3847/1538-4357/ad8448](https://doi.org/10.3847/1538-4357/ad8448)
- Whipple, F. L. 1950, *ApJ*, 111, 375, doi: [10.1086/145272](https://doi.org/10.1086/145272)
- . 1951, *ApJ*, 113, 464, doi: [10.1086/145416](https://doi.org/10.1086/145416)
- Xing, Z., Bodewits, D., Noonan, J., & Bannister, M. T. 2020, *ApJ*, 893, L48, doi: [10.3847/2041-8213/ab86be](https://doi.org/10.3847/2041-8213/ab86be)
- Xing, Z., Oset, S., Noonan, J., & Bodewits, D. 2025, arXiv e-prints, arXiv:2508.04675, doi: [10.48550/arXiv.2508.04675](https://doi.org/10.48550/arXiv.2508.04675)
- Yaginuma, A., Taylor, A. G., & Seligman, D. Z. 2025, arXiv e-prints, arXiv:2510.25945, doi: [10.48550/arXiv.2510.25945](https://doi.org/10.48550/arXiv.2510.25945)
- Yang, B., Kelley, M. S. P., Meech, K. J., et al. 2020, *A&A*, 634, L6, doi: [10.1051/0004-6361/201937129](https://doi.org/10.1051/0004-6361/201937129)
- Yang, B., Meech, K. J., Connelley, M., & Keane, J. V. 2025, arXiv e-prints, arXiv:2507.14916, <https://arxiv.org/abs/2507.14916>
- Yang, B., Li, A., Cordiner, M. A., et al. 2021, *Nature Astronomy*, doi: [10.1038/s41550-021-01336-w](https://doi.org/10.1038/s41550-021-01336-w)
- Ye, Q., Kelley, M. S. P., Bolin, B. T., et al. 2020, *AJ*, 159, 77, doi: [10.3847/1538-3881/ab659b](https://doi.org/10.3847/1538-3881/ab659b)
- Ye, Q., Kelley, M. S. P., Hsieh, H. H., et al. 2025, arXiv e-prints, arXiv:2509.08792, doi: [10.48550/arXiv.2509.08792](https://doi.org/10.48550/arXiv.2509.08792)
- Ye, Q.-Z., Zhang, Q., Kelley, M. S. P., & Brown, P. G. 2017, *ApJ*, 851, L5, doi: [10.3847/2041-8213/aa9a34](https://doi.org/10.3847/2041-8213/aa9a34)

This paper was built using the Open Journal of Astrophysics L^AT_EX template. The OJA is a journal which

provides fast and easy peer review for new papers in the **astro-ph** section of the arXiv, making the reviewing process simpler for authors and referees alike. Learn more at <http://astro.theoj.org>.